Chinese Chemical Letters 33 (2022) 3931–3935

Contents lists available at ScienceDirect

Chinese Chemical Letters

journal homepage: www.elsevier.com/locate/cclet

Design of hierarchical and mesoporous FeF_3/rGO hybrids as cathodes for superior lithium-ion batteries

Jiale Lian[a], Yang Wu[a], Yichuan Guo[a], Zhenyun Zhao[a], Qinghua Zhang[b], Yang Hou[b], Lingxiang Chen[c], Bin Lu[a,d], Xinhua Pan[a,d], Zhizhen Ye[a,d], Jianguo Lu[a,d,*]

[a] State Key Laboratory of Silicon Materials, Key Laboratory for Biomedical Engineering of Ministry of Education, School of Materials Science and Engineering, Zhejiang University, Hangzhou 310027, China
[b] College of Chemical and Biological Engineering, Zhejiang University, Hangzhou 310027, China
[c] Key Laboratory for Biomedical Engineering of Ministry of Education, College of Biomedical Engineering and Instrument Science, Zhejiang University, Hangzhou 310027, China
[d] Wenzhou Key Laboratory of Novel Optoelectronic and Nano Materials, Institute of Wenzhou, Zhejiang University, Wenzhou 325006, China

ARTICLE INFO

Article history:
Received 7 October 2021
Revised 12 November 2021
Accepted 6 December 2021
Available online 12 December 2021

Keywords:
Li-ion batteries
Transition metal fluorides
Reduced graphite oxide
Hybrid electrodes
In-situ synthesis
High-temperature operation

ABSTRACT

Iron fluoride (FeF_3) is considered as a promising cathode material for Li-ion batteries (LIBs) due to its high theoretical capacity (712 mAh/g) with a $3e^-$ transfer. Herein, we have designed a strategy of hierarchical and mesoporous FeF_3/rGO hybrids for LIBs, where the hollow FeF_3 nanospheres are the main contributor to the specific capacity and the 2D rGO nanosheets are the matrix elevating the electronic conductivity and buffering the volume expansion. The unique FeF_3/rGO hybrid can be rationally synthesized by a non-aqueous *in-situ* precipitation method, offering the merits of large specific surface area with rich active sites, fast transport channels for lithium ions, effective alleviation of volume expansion during cycles, and accelerating the electrochemical reaction kinetics. The FeF_3/rGO hybrid electrode possesses a high initial discharge capacity of 553.9 mAh/g at a rate of 0.5 C with 378 mAh/g after 100 cycles, acceptable rate capability with 168 mAh/g at 2 C, and feasible high-temperature operation (320 mAh/g at 70 °C). The superior electrochemical behaviors presented here demonstrates that the FeF_3/rGO hybrid is a potential electrode for LIBs, which may open up a new vision to design high-efficiency energy-storage devices such as LIBs based on transition metal fluorides.

The past decade has seen the rapid development of electric vehicles and portable electronic devices, and the need for energy storage equipment has become more urgent [1–3]. Lithium-ion batteries (LIBs) are the popularly used energy storage device in commercial [4,5]. Co- and Ni- based intercalation-type cathodes are generally employed in LIBs [6–9], which can ensure the reversibility. Ni-rich layered materials ($LiNi_{1-x}M_xO_2$, M = Co, Mn and Al) have the specific capacity higher than 180 mAh/g. Even so, the capacity of cathodes is still the main obstacle for LIBs [10–12]. Also, the resources of Co, Ni and Mn are limited. Therefore, researchers have shown an increased interest to explore new cathode materials for the breakthrough in performance of LIBs.

More recently, transition metal fluorides (TMFs) have attracted great attention as a cathode material for LIBs [13–17]. Among them, iron fluoride (FeF_3) is considered as a promising candidate [18–22], since it has a large theoretical energy density (712 mAh/g, $3e^-$ transfer) and high electromotive force (EMF) of 2.7 V [23], as well as the abundance in Earth's crust, low cost, and friendliness to the environment of Fe [24]. However, FeF_3 has its limitations, such as the poor electronic conductivity derived from the wide-bandgap of Fe-F bonds, which leads to its low specific capacity far below the theoretical value and poor rate capability [25–27]. To overcome the drawbacks of iron fluoride electrodes, two approaches have been proposed: one is decreasing the size of grains with nanoscale structures [28–31], and another is compositing with high conductivity materials [32–36]. Naturally, it is an ideal approach to *in-situ* synthesize hybrids consisting of iron-based fluorides and conductive additives with hierarchical and mesoporous nanostructure, which, however, is still an unresolved issue to be overcome for practical applications.

In this work, we have elaborately designed a hybrid of hollow FeF_3 nanospheres and 2D reduced graphene oxide (rGO) nanosheets, and developed a non-aqueous *in-situ* precipitation method to rationally synthesize the FeF_3/rGO hybrids. In the solvothermal process, the Fe^{3+} of precursor was introduced to a

* Corresponding author.
E-mail address: lujianguo@zju.edu.cn (J. Lu).

https://doi.org/10.1016/j.cclet.2021.12.014
1001-8417/

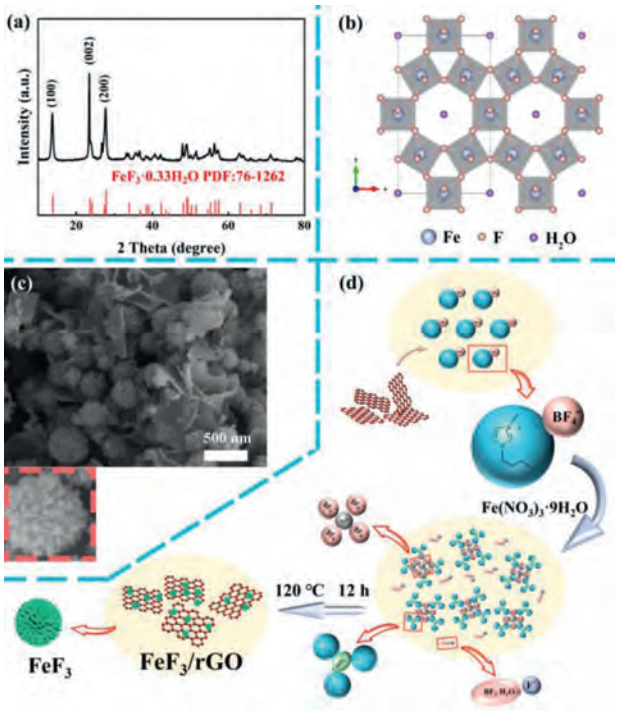

Fig. 1. (a) XRD spectra of FeF_3/rGO hybrids. (b) Crystal structure of FeF_3 with HTB phase. (c) SEM images of FeF_3/rGO hybrids, where the inset shows the enlarged image of a single FeF_3 nanosphere. (d) Schematic diagram of formation process of FeF_3/rGO hybrids.

GO dispersion. Because the surface of GO contains a large number of oxygen-containing sites which have a strong affinity with Fe^{3+} cations, the synthesized FeF_3 nanospheres are hierarchical and mesoporous [37]. The unique FeF_3/rGO nano-architectures with a hollow mesoporous structure is endowed with the large specific surface area and rich voids, which provides sufficient space to electrolyte penetration and alleviate the volume variation of active materials during the process of lithium intercalation and deintercalation. Consequently, the FeF_3/rGO hybrid electrode delivers a high initial discharge capacity of 553.9 mAh/g at a rate of 0.5 C with an acceptable cycling stability (378 mAh/g after 100 cycles at 0.5 C) and rate capability (168 mAh/g at 2 C), and outstanding high-temperature behaviors (320 mAh/g at 70 °C) as well. Our study presented in this work may open the door to design superior transition metal fluoride electrodes for advanced LIBs for next-generation energy storage.

The crystal structures of FeF_3 and FeF_3/rGO hybrids were characterized by X-ray diffraction (XRD), as shown in Fig. S1 (Supporting information) and Fig. 1a, respectively. In both cases, all the diffraction peaks can be attributed to orthorhombic $FeF_3{\cdot}0.33H_2O$ (JCPDS No. 76–1262). Among them, the diffraction peaks at $2\theta = 13.8°$, 23.6° and 27.8° are matched to the (110), (002) and (220) planes of $FeF_3{\cdot}0.33H_2O$, respectively. The diffraction peak of rGO cannot be detected in the XRD spectra, suggesting that the rGO is of a typical amorphous carbon shape. In the $FeF_3{\cdot}0.33H_2O$ structure (Fig. 1b), six FeF_6 octahedrons composing a special large hexagonal cavity through the corner-sharing, forming a large cell volume [38]. Although only a small amount of water existing in the center of the hexagonal cavity, water molecules play a structural stabilizer role in $FeF_3{\cdot}0.33H_2O$ lattice, stabilizing the large hexagonal cavity and avoiding the structural collapse of iron fluoride during lithium ion's insertion and extraction [39–41]. On the other hand, water molecules can also increase the tunnel size of the crystal, which is beneficial in the rapid diffusion of lithium ions.

The morphologies of FeF_3 and FeF_3/rGO hybrids were characterized by scanning electron microscopy (SEM). Fig. S2 (Supporting information) shows the SEM image of FeF_3, displaying nanoscale spherical structure with uniform shape and size. Fig. 1c shows the SEM image of FeF_3/rGO hybrids. Similarly, the FeF_3 displays nanospherical structure with uniform shape and size in hybrids, and the FeF_3 nanospheres are dispersed among three-dimensional (3D) rGO framework in a relatively homogenous manner. At higher magnifications (inset of Fig. 1c), it can be observed that the FeF_3 nanospheres are quite regular in shape with a diameter of about 500 nm, which is further assembled by a mass of primary nanoparticles with variable sizes. The tiny primary nanoparticles are gathered with intermediate pores between them, giving rise to the mesoporous structure of FeF_3 nanospheres. The secondary, mesoporous, and 3D nanostructures of FeF_3/rGO hybrids are in favor of the access of the electrolyte to the electrode surface.

The formation mechanism of FeF_3/rGO hybrids was proposed in Fig. 1d. The procedure begins with the dispersion of the graphene *via* interactions between the imidazolium cation group of the IL BMIM[BF_4] and the π-electrons of graphene after adding extra graphene. Thus, the FeF_3 particles can firmly anchor on the surface of the graphene. Then adding $Fe(NO_3)_3{\cdot}9H_2O$ powder as the iron source into the BMIM[BF_4] and GO solution, a serious reaction will happen. Firstly, the hydration water is separated from the $Fe(NO_3)_3{\cdot}9H_2O$ and enters into the hydrophilic IL medium [42,43]. At the same time, Fe^{3+} and NO_3^- are coordinatedly surrounded by BF_4^- anions and imidazolium cations, respectively. Furthermore, with the existence of hydration water, some weakly coordinated BF_4^- anions are easy to hydrolyze and release $BF_3{\cdot}H_2O$ and F^- under heating condition. Finally, the solvated Fe^{3+} combines with the F^- to form precipitated iron-based fluorides nanoparticles. With the increasing reaction time, the growth of well-separated spherical-like crystals from those of smaller size happens due to the Ostwald ripening process. Besides, the interior space emerges within the larger particles and the hollow structure obtained in apart of $FeF_3{\cdot}0.33H_2O$. It is believed that the formation approach provided here are universal and promising in the synthesis of iron-based fluorides, since it is thought to be simple and environmentally friendly.

Fig. 2a shows transmission electron microscopy (TEM) image of the FeF_3/rGO hybrids. The FeF_3 nanospheres can be clearly identified in hybrids, which are hollow with rather rough surface. Enlarged TEM image (Fig. 2b) further displays that the rough surface of FeF_3 nanospheres has a neat morphology, which is assembled by a mass of tiny nanoparticles with sizes ranging from 10 nm to 20 nm. The rGO nanosheets can be readily observed, as displayed in Fig. S3 (Supporting information), which are entangled with FeF_3 nanospheres tightly. In what follows we mainly focus on the microstructures of FeF_3 nanospheres. The special structure of FeF_3 nanospheres is believed to be the result of Ostwald ripening process [44,45]. In brief, this process involves the growth of larger crystals from those of smaller size which have a higher solubility than the larger ones, so the inside-out Ostwald ripening induces the transformation of mesoporous structure from the solid particles and the outward Ostwald ripening results in the formation of hollow structure from the spheres. The lattice fringes in the HRTEM image (Fig. 2c) reveals the crystalline nature of FeF_3. The lattice spacing of 0.3664 nm is assigned to the (020) plane of FeF_3. The selected area electron diffraction (SAED) pattern is shown in Fig. 2d. It can be seen that the diffraction spots and diffraction rings coexist, indicating that the polycrystalline nature of FeF_3 in the hybrids. Fig. 2e shows the EDS elemental mapping of FeF_3 nanospheres. The elements of Fe, F and O exhibit a homogeneous distribution, indicating that the product is a pure hydrated

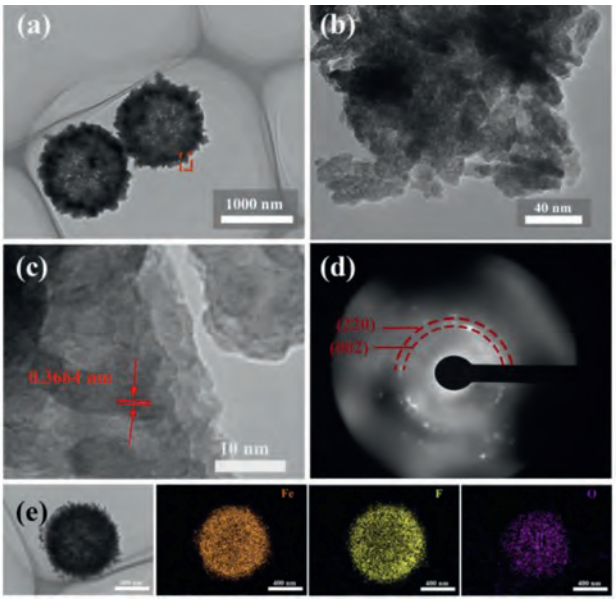

Fig. 2. (a-c) TEM images of FeF_3/rGO hybrids at different magnifications. (d) SAED patterns of FeF_3/rGO hybrids. (e) TEM image of FeF_3 nanosphere and the corresponding EDS mapping of Fe, O and C elements.

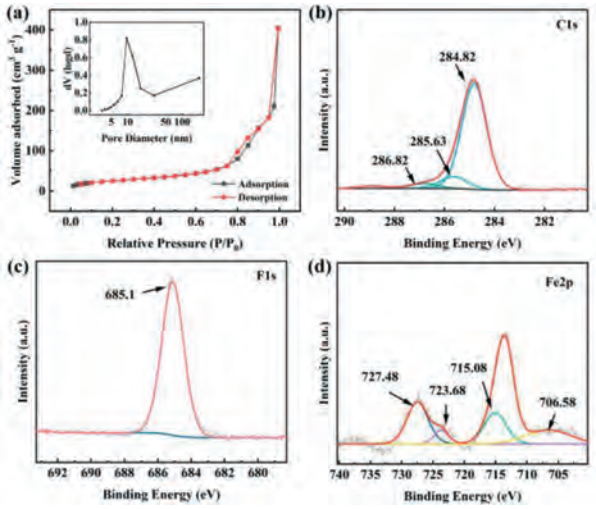

Fig. 3. (a) Nitrogen adsorption–desorption isotherm and pore size distribution (inset) curve of FeF_3/rGO hybrids. (b) C 1s, (c) F 1s, and (d) Fe 2p XPS spectra of FeF_3/rGO hybrids.

iron based fluoride without any impurities. The structures of FeF_3 nanospheres demonstrated above may play threefold roles at least: (1) The nanoparticles are cross-linked each other in an irregular manner leaving plenty of interspaces with mesopores, which can facilitate the infiltration of electrolyte into the inside of electrode [46]; (2) The hollow structure provides a thin and porous shell, large internal void, and double surfaces, which can ensure the high surface area with short transport length for Li ions; (3) The hollow core can buffer the volume changes effectively during the insertion/extraction of Li ions. Undoubtedly, based on the SEM and TEM observations, the FeF_3/rGO hybrids are of hierarchical, hollow and mesoporous nanostructures, which will certainly enhance the electrochemical behaviors for energy storage.

The pore size distribution and specific surface area of hybrids were analyzed by taking nitrogen adsorption-desorption measurement. As shown in Fig. 3a, according to IUPAC classification, the nitrogen adsorption-desorption curve of FeF_3/rGO hybrid shows

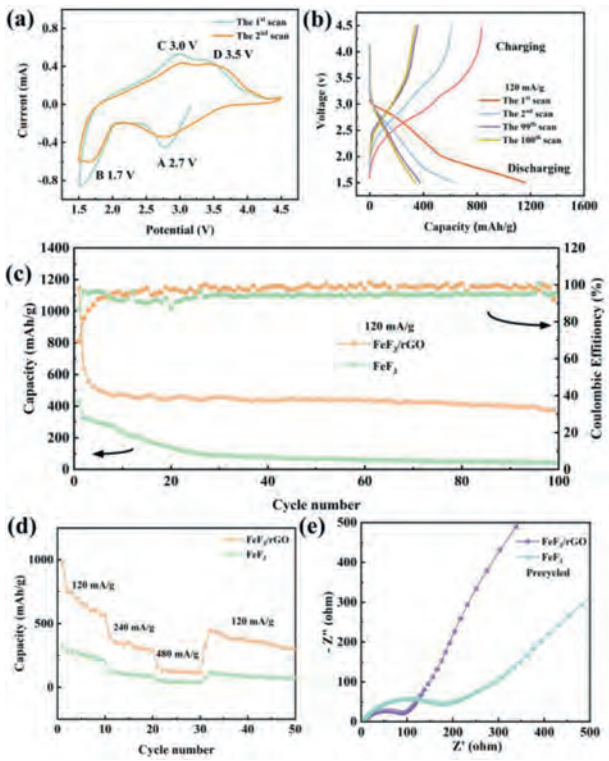

Fig. 4. (a) CV profiles and (b) charge-discharge curves of FeF_3/rGO hybrids. (c) Cycle performance of FeF_3 and FeF_3/rGO at 0.5 C. (d) Rate performance of FeF_3 and FeF_3/rGO. (e) Nyquist plots of FeF_3 and FeF_3/rGO hybrids.

a typical type IV isotherm, with a capillary condensation phenomenon [47]. By Brunauer–Emmett–Teller (BET) method, the specific surface area is calculated to be 91.92 m^2/g for the FeF_3/rGO hybrid (Table S1 in Supporting information). The Barrett–Joyner–Halenda (BJH) results indicate that most of the pore sizes are fall into the range of 8–11 nm in distribution. As displayed in Fig. S4 (Supporting information), the FeF_3 nanospheres have a BET specific surface area of 55.13 m^2/g and an average pore size of 9.57 nm. It is evidently that the specific surface area has been elevated for the products after compositing rGO to FeF_3, which is beneficial to provide high contact area and a large number of active sites of charge transfer reaction [48].

In order to gain more insight into the chemical states of elements in the FeF_3/rGO hybrid, XPS measurements are carried out and the corresponding spectra are shown in Fig. S5 (Supporting information). There are obvious signals of C, F and Fe elements. The signal of C 1s (Fig. 3b) with three peaks at 284.8, 285.6 and 286.8 eV are attributed to the benchmark carbon, the C–O and C=O in rGO, respectively [49]. The binding energy (Fig. 3c) on the basic of F 1s spectrum is 685.1 eV, which is closely matches with metal fluorides. For Fe 2p spectrum, there are two obvious peaks (Fig. 3d) at 715.1 eV and 727.5 eV, arising from Fe $2p_{3/2}$ and Fe $2p_{1/2}$, respectively, which indicate the Fe^{3+} oxidation state of iron and are consistent with the characteristic peak of Fe-F.

The cycle voltammetry was measured at a scanning rate of 0.5 mV/s in the voltage range 1.5~4.5 V (*vs.* Li^+/Li). The CV curves for the synthesized FeF_3/rGO hybrids are exhibited in Fig. 4a. In the cathodic process, there are two pairs of redox peaks observed in the CV curve, one is the reduction peak position at about 2.7 V, which may be ascribed to the Li^+ insertion process between phases containing Fe^{3+} and Fe^{2+}, and another one is the reduction peak existing at about 1.7 V, which can be attributed to the reversible conversion reaction between phase containing Fe^{2+} and

metallic Fe^0 [26]. Apparently, Li^+ is more likely to insert into FeF_3 step by step as described in the following Eqs. 1 and 2.

$$FeF_3 + Li \rightarrow LiFeF_3 \quad (4.5–1.7\,V) \tag{1}$$

$$LiFeF_3 + 2Li \rightarrow Fe + 3LiF \quad (1.7–1.5\,V) \tag{2}$$

Fig. S6a (Supporting information) shows the CV curves of the FeF_3 nanospheres. By comparing the CV curves in Fig. 4a and Fig. S6a, the FeF_3/rGO hybrid has a higher capacity clearly. In the subsequent cycles, the CV profiles of the FeF_3/rGO hybrid are basically coincident, revealing the stability of electrode with tiny capacity attenuation.

Further, the charge-discharge cyclic measurements were carried out in the voltage range of 1.5–4.5 V at a current density of 120 mA/g (defined as 0.5 C). As shown in Fig. 4b, the voltage profile of FeF_3/rGO has a two-stage electrochemical reaction mechanism at the first discharge process between 1.5 V and 4.5 V. The two discharge voltage plateaus appearing at 2.9 and 1.6 V are corresponding to intercalation and conversion reactions, respectively, according to the CV (Fig. 4a) and Eqs. 1 and 2. From the GCD curves, it can be seen that the discharge capacity gradually decreases in the first 10 cycles, and a relatively stable capacity can be maintained during the subsequent cycles. As delivered in Fig. 4b, the FeF_3/rGO hybrid demonstrates a discharge capacity of 1158 mAh/g at the first cycle, which is evidently higher than that of FeF_3 (430.9 mAh/g) in Fig. S6b (Supporting information). Note that the 1158 mAh/g is clearly beyond the theoretical value of FeF_3 (712 mAh/g), which may be owing to the low and long plateau observed during the first discharge and the formation of SEI film.

Fig. 4c shows the long-term cycling stability of both FeF_3 and FeF_3/rGO hybrids at 0.5 C. For the FeF_3/rGO hybrid, the specific capacity is around 1158 mAh/g at the first cycle. It is reduced to 553.9 mAh/g at the third cycle, which is a reasonable value, and for cautiousness, it is considered as the initial specific capacity. The specific capacity is further reduced to 480 mAh/g after 10 cycles and then keeps stable in the main, with the specific capacity of 380 mAh/g still remained after 100 cycles. In contrast, the bare FeF_3 displays a poor capacity of 45 mAh/g after 100 cycles. The decrease of specific capacity in the initial cycles is probably due to the long low-voltage plateau in the initial discharge curves and the formation of SEI layer related to the adverse reactions between electrode and electrolyte [48,50,51]. Similarly, the coulombic efficiency of the FeF_3/rGO hybrid electrodes increases immediately on the second cycle, exceeding 98% within the first 10 cycles, and remains very close to 100% after that. In general, the coulombic efficiency of the FeF_3/rGO hybrid is significantly higher than that of pure FeF_3 during the electrochemical process, which is ascribed to the high Li^+ and electronic conductivity of hybrids.

Based on the above results, we can now know that the FeF_3/rGO hybrid has an evidently higher specific capacity, higher columbic efficiency, and longer cycling lifetime. Naturally, it can be attributed to the introduction of rGO in the hybrid. The introduced rGO layer may play multiple roles, such as increasing the conductivity, buffering the volume variation, reducing the polarization of FeF_3, providing efficient access for Li^+ into the spherical particle, and facilitating electron transport to the surface of the active material [52–54]. In the FeF_3/rGO hybrid, the hollow FeF_3 nanospheres are the main contributor to the specific capacity, and the contribution of rGO to the overall electrode capacity is negligible, as identified in shown in Fig. S7 (Supporting information). The surface morphology of the FeF_3/rGO hybrid electrode displays no obvious change before and after cycles, as displayed in Fig. S8 (Supporting information). The sphere-like particles still maintain a complete shape and smooth surface, which ensures the structural stability and that the electrode expansion is not serious.

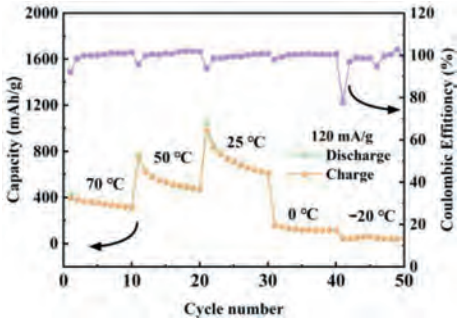

Fig. 5. Specific capacity of FeF_3/rGO hybrids at 0.5 C in a wide temperature range from −20 °C to 70 °C.

Fig. 4d shows the comparison of the rate capability for the FeF_3 nanosphere and FeF_3/rGO hybrids. Fig. S9 (Supporting information) displays the GCD curves at different current densities. Compared with the FeF_3, the rate capability of FeF_3/rGO hybrid is apparently im proved at high rates. In particular, the discharge capacity of FeF_3/rGO hybrid electrode attains around 600 mAh/g at 0.5 C, and the capacity retentions are about 390 and 168 mAh/g at 1 C and 2 C, respectively. When the current density was reset to its initial value of 0.5 C after deep cycling, the discharge capacity of 467 mAh/g can still be recovered. In contrast, the FeF_3 only provides a discharge capacity of 340 mAh/g at 0.5 C, which fades gradually at higher current densities and the recovered value is only 124 mAh/g at 0.5 C. The favorable rate performance is also attributed to the rGO modification in the FeF_3/rGO hybrids.

Fig. 4e displays the electrochemical impedance spectra (EIS) of FeF_3 and FeF_3/rGO hybrids. The impedance spectra of two cases both consist of one semicircle located in the high-frequency region and a liner trail position at the low-frequency region [55]. Usually, the semicircle is relevant to the charge-transfer diffusion resistance (R_{CT}) and the sloping line is relevant to the lithium diffusion process within the electrode [56]. Apparently, the FeF_3/rGO hybrid electrode shows a smaller diameter of semicircle than the FeF_3 electrode. The smaller diameter of the semicircle in high frequency implies that the FeF_3/rGO electrode possesses a high electron conductivity and a rapid charge transfer reaction. The EIS profiles of FeF_3/rGO electrode operated after the 3rd, 50th and 100th circles are shown in Fig. S10 (Supporting information). The resistance gradually increases with the increase of the number of cycles, indicating that the electrode still suffers from the irreversible structural degradation. This also explains why the capacity of the electrode decays with cycles. The result agrees with the electrochemical behaviors observed above for the FeF_3/rGO hybrid electrodes.

To further explore the electrochemical activity of the FeF_3/rGO hybrid, we carried out the high/low temperature measurements at 0.5 C for LIBs assembled with FeF_3/rGO hybrid electrodes, as shown in Fig. 5. The FeF_3/rGO hybrid electrode shows the capacities of ~320, 480, 615, 120 and 45 mAh/g at 70, 50, 25, 0 and −20 °C, respectively. Although the low-temperature operation of the FeF_3/rGO LIBs is not acceptable, it can work well at high temperatures. It is well known that the ionic and electronic conductivity decreases at low temperatures, which may be vital for the FeF_3 LIB, resulting in the low capacity and poor stability of battery [57,58]. At high temperatures, the electrode can provide sufficient pathways for achieving fast electron transfer and Li ion diffusion, which offers improved reaction kinetics for electrochemical performance; at the same time the electrolyte decomposition occurs and the passivation layer is formed on the surface of electrode as the temperature increases, so the reaction kinetics is restrained by the size of the active domains [59]. Under the interaction of

the above two factors, the LIBs generally reach the highest capacity at a certain temperature, which is room temperature (25 °C) for the FeF_3/rGO hybrid LIBs in our cases. As demonstrated above, the specific capacity is around 320 mAh/g at 70 °C, with a capacity decay of only ~50% as compared with that at room temperature. The FeF_3/rGO hybrid may be an ideal high-temperature electrode for LIBs.

In summary, we have proposed a hierarchical and mesoporous hybrid with hollow FeF_3 nanospheres and 2D rGO nanosheets for LIBs. Also, we have developed a facile, harmless, and environmentally friendly non-aqueous method to rationally synthesize the FeF_3/rGO hybrids. The as-synthesized FeF_3/rGO hybrids have a high specific surface area of 94 m^2/g, exhibiting a high initial discharge capacity (553.9 mAh/g at 0.5 C) with acceptable cycle performance (residual capacity of 378 mAh/g after 100 cycles). Notedly, the LIBs assembled with FeF_3/rGO hybrid electrodes can work well from room temperature to high temperatures, with a very high specific capacity of 320 mAh/g at 70 °C. The electrochemical behaviors of FeF_3/rGO hybrids are improved evidently as compared to pure FeF_3 nanostructures. The superior performance presented here for the hybrid is attributed to not only the unique hollow mesoporous FeF_3 nanospheres that is beneficial to enhance the structure stability and shortening the Li^+ transport path, but also the rGO layers that facilitate electron transport to the surface of FeF_3 and provide Li^+ with efficient access into the structure. It is expected that the FeF_3/rGO hybrid will be a promising cathode material for energy storage devices such as advanced LIB systems.

Declaration of competing interest

The authors declare no conflict of interest.

Acknowledgments

This work was financially supported by National Natural Science Foundation of China (No. U20A20209), Zhejiang Provincial Key Research and Development Program (No. 2021C01030), Zhejiang Provincial Natural Science Foundation of China (No. LD19E020001), and Open Project of Laboratory for Biomedical Engineering of Ministry of Education, Zhejiang University.

Supplementary materials

Supplementary material associated with this article can be found, in the online version, at doi:10.1016/j.cclet.2021.12.014.

References

[1] B. Xu, D.N. Qian, Z.Y. Wang, Y.S.L. Meng, Mater. Sci. Eng. R 73 (2012) 51–65.
[2] H.C. Tang, K.Q. Xia, J.G. Lu, et al., Nano Energy 84 (2021) 105931.
[3] X. Teng, X. Sun, L. Guan, et al., Tungsten 2 (2020) 337–361.
[4] J.B. Goodenough, Y. Kim, Chem. Mater. 22 (2009) 587–603.
[5] X. Liu, L. Li, G. Li, Tungsten 1 (2019) 276–286.
[6] L.X. Yuan, Z.H. Wang, W.X. Zhang, et al., Energy Environ. Sci. 4 (2011) 269–284.
[7] Z. Jian, W. Wang, M. Wang, et al., Chin. Chem. Lett. 29 (2018) 1768–1772.
[8] W. Lee, S. Muhammad, C. Sergey, et al., Angew. Chem. Int. Ed. 59 (2020) 2578–2605.
[9] W. Li, B. Song, A. Manthiram, Chem. Soc. Rev. 46 (2017) 3006–3059.
[10] H. Li, P. Balaya, J. Maier, J. Electrochem. Soc. 151 (2004) A1878–A1885.
[11] Y. Yang, L. Gao, L. Shen, N. Bao, J. Alloys Compd. 873 (2021) 159799.
[12] X. Xi, Y. Fan, Y. Liu, et al., J. Alloys Compd. 872 (2021) 159664.
[13] Y. Bai, X. Zhou, Z. Jia, et al., Nano Energy 17 (2015) 140–151.
[14] W. Zhang, L. Ma, H.J. Yue, Y. Yang, J. Mater. Chem. 22 (2012) 24769–24775.
[15] J.K. Seo, H.M. Cho, K. Takahara, et al., Nano Res. 10 (2017) 4232–4244.
[16] D.T. Thieu, M. Hammad, H. Bhatia, et al., Adv. Funct. Mater. 27 (2017) 1701051.
[17] A. Kitajou, K. Eguchi, Y. Ishado, et al., J. Power Sources 419 (2019) 1–5.
[18] C.L. Li, X.K. Mu, P.A. van Aken, J. Maier, Adv. Energy. Mater. 3 (2013) 113–119.
[19] M. Nishijima, I.D. Gocheva, S. Okada, et al., J. Power Sources 190 (2009) 558–562.
[20] S.W. Kim, D.H. Seo, H. Gwon, et al., Adv. Mater. 22 (2010) 5260–5264.
[21] D. Cao, C. Yin, D. Shi, et al., Adv. Funct. Mater. 27 (2017) 1701130.
[22] Y. Han, J. Hu, C. Yin, et al., J. Mater. Chem. A 4 (2016) 7382–7389.
[23] F. Badway, F. Cosandey, N. Pereira, G.G. Amatucci, J. Electrochem. Soc. 150 (2003) A1318–A1327.
[24] J.L. Tan, L. Liu, S.P. Guo, et al., Electrochim. Acta 168 (2015) 225–233.
[25] H. Arai, S. Okada, Y. Sakurai, J. Yamaki, J. Power Sources 68 (1997) 716–719.
[26] R.F. Li, S.Q. Wu, Y. Yang, Z.Z. Zhu, J. Phys. Chem. C 114 (2010) 16813–16817.
[27] M.J. Zhou, L.W. Zhao, T. Doi, et al., J. Power Sources 195 (2010) 4952–4956.
[28] R. Zhang, X. Wang, S. Wei, et al., J. Alloys Compd. 719 (2017) 331–340.
[29] L. Li, F. Meng, S. Jin, Nano Lett 12 (2012) 6030–6037.
[30] B.J. Li, Z.J. Cheng, N.Q. Zhang, K.N. Sun, Nano Energy 4 (2014) 7–13.
[31] S. Wei, X. Wang, M. Jiang, et al., J. Alloys Compd. 689 (2016) 945–951.
[32] B. Li, N. Zhang, K. Sun, Small 10 (2014) 2039–2046.
[33] Q. Zhang, N.N. Liu, C.Z. Sun, et al., ChemElectroChem 6 (2019) 2189–2194.
[34] X.B. Hu, M.H. Ma, R.G. Mendes, et al., J. Mater. Chem. A 3 (2015) 23930–23935.
[35] Q. Zhang, C. Sun, L. Fan, et al., Chem. Eng. J. 371 (2019) 245–251.
[36] R. Zhang, X. Wang, X. Wang, et al., J. Electrochem. Soc. 165 (2018) A89–A96.
[37] Y. Chu, B. Xi, S. Xiong, Chin. Chem. Lett. 32 (2021) 1983–1987.
[38] C. Li, C. Yin, L. Gu, et al., J. Am. Chem. Soc. 135 (2013) 11425–11428.
[39] C.L. Li, L. Gu, J.W. Tong, et al., Adv. Funct. Mater. 21 (2011) 1391–1397.
[40] L. Liu, H. Guo, M. Zhou, et al., J. Power Sources 238 (2013) 501–515.
[41] J. Hu, Y. Zhang, D. Cao, C. Li, J. Mater. Chem. A 4 (2016) 16166–16174.
[42] M.L. Jiang, X.Y. Wang, Y.Q. Shen, et al., Electrochim. Acta 186 (2015) 7–15.
[43] C. Li, L. Gu, S. Tsukimoto, et al., Adv. Mater. 22 (2010) 3650–3654.
[44] Y. Lu, Z. Wen, J. Jin, et al., Phys. Chem. Chem. Phys. 16 (2014) 8556–8562.
[45] J. Liu, W. Liu, S. Ji, et al., Chem. Eur. J. 20 (2014) 5815–5820.
[46] Y. Tian, Z. Wang, J. Fu, et al., Chem. Commun. 55 (2019) 10960–10963.
[47] R.G. Ma, M. Wang, P.P. Tao, et al., J. Mater. Chem. A 1 (2013) 15060–15067.
[48] Y. Guo, Z. Wang, X. Lu, et al., Chem. Commun. 56 (2020) 1980–1983.
[49] C. Hao, T. Gao, A. Yuan, J. Xu, Chin. Chem. Lett. 32 (2021) 113–118.
[50] W.T. Gu, O. Borodin, B. Zdyrko, et al., Adv. Funct. Mater. 26 (2016) 1507–1516.
[51] P. Liu, J.J. Vajo, J.S. Wang, et al., J. Phys. Chem. C 116 (2012) 6467–6473.
[52] F. Wu, V. Srot, S. Chen, et al., Adv. Mater. 31 (2019) 1905146.
[53] T. Kim, W.J. Jae, H. Kim, et al., J. Mater. Chem A 4 (2016) 14857–14864.
[54] G. Xiang, J. Yin, X. Zhang, et al., Chin. Chem. Lett. 32 (2021) 2169–2173.
[55] Y.L. Shi, M.F. Shen, S.D. Xu, et al., Solid State Ionics 222 (2012) 23–30.
[56] T.L. Zhao, L. Li, R.J. Chen, et al., Nano Energy 15 (2015) 164–176.
[57] Y. Na, X. Sun, A. Fan, et al., Chin. Chem. Lett. 32 (2021) 973–982.
[58] Y. Tian, J. Lu, H. Tang, et al., Chem. Eng. J. 422 (2021) 130054.
[59] H. Chen, R. Liu, Y. Wu, et al., Chem. Eng. J. 407 (2021) 126973.